Nanoscale Research Letters

NANO EXPRESS

Open Access

CrossMark

Electrodeposition of SnO2 on FTO and its Application in Planar Heterojunction Perovskite Solar Cells as an Electron Transport Layer

Yohan Ko[1], Yeong Rim Kim[1], Haneol Jang[1], Chanyong Lee[1], Man Gu Kang[2] and Yongseok Jun[1*]

Abstract

We report the performance of perovskite solar cells (PSCs) with an electron transport layer (ETL) consisting of a SnO_2 thin film obtained by electrochemical deposition. The surface morphology and thickness of the electrodeposited SnO_2 films were closely related to electrochemical process conditions, i.e., the applied voltage, bath temperature, and deposition time. We investigated the performance of PSCs based on the SnO_2 films. Remarkably, the experimental factors that are closely associated with the photovoltaic performance were strongly affected by the SnO_2 ETLs. Finally, to enhance the photovoltaic performance, the surfaces of the SnO_2 films were modified slightly by $TiCl_4$ hydrolysis. This process improves charge extraction and suppresses charge recombination.

Keywords: SnO_2, Electrodeposition, Perovskite solar cell, Electrochemistry

Background

Solar cell devices based on organometallic perovskite materials have exhibited unprecedented performance over the brief span of 6 years, and organometallic halide perovskite solar cells (PSCs) show promise as affordable alternative solar cells with high power conversion efficiency (PCE) [1–3]. The huge interest in this new class of solar cells is due to their high absorption coefficient, ambipolar charge transport, small exciton binding energy, and long diffusion length [4–6]. Despite these excellent properties, PSCs possess several drawbacks. The most important of these are the sensitivity of perovskite materials to moisture, heat, and UV irradiation. To address these drawbacks, it has been found that adding formamidinium and/or an inorganic cation (Cs or Rb) to a methylammonium cation improves the stability against these environmental factors [3], and the durability of PSCs thus depends on both the device configuration (n-i-p, p-i-n) and the metal oxide semiconductors [7]. Generally, TiO_2 materials are widely used in

PSCs as electron transport layers (ETLs) in the n-i-p device configuration because of their large band gap and band alignment, and highly efficient PSCs are realized using TiO_2 ETLs [8]. Although PSCs with TiO_2 ETLs exhibit remarkable efficiency, the UV sensitivity and electronic properties of TiO_2 have been suggested as targets for improvement to reduce the hysteresis and obtain durable PSCs [9]. Specifically, Heo et al. reported that Li doping can enhance the carrier mobility and conductivity of TiO_2 and thus yield PSCs without significant hysteresis [10]. Ito et al. reported that when TiO_2 in a PSC is exposed to UV irradiation, electrons are extracted at the TiO_2/perovskite interface, degrading the perovskite material [11].

Stannic oxide (SnO_2) has been widely studied for diverse applications such as batteries, gas sensors [12], solar cells [13], and catalysts. It is regarded as a promising candidate for use as a transparent conducting material and photoelectrode in photovoltaic devices. Considerable attention has been drawn recently to its application in PSCs as an alternative ETL with the goal of enhancing device performance and light stability, as it has a larger band gap (~3.6 eV at 300 K), higher electrical conductivity, and greater chemical stability than

* Correspondence: yjun@konkuk.ac.kr
[1]Department of Materials Chemistry and Engineering, Department of Energy Engineering, Konkuk University, Seoul 143-701, Republic of Korea
Full list of author information is available at the end of the article

Ko et al. Nanoscale Research Letters (2017) 12:498

Page 2 of 7

TiO$_2$ semiconductors [2]. Various synthetic routes to SnO$_2$, including sol–gel methods [14], molten-salt synthesis [15], microwave techniques [16], atomic layer deposition (ALD), and electrochemical deposition (ED) [17–20] have been developed. ALD and spin-coating solution processes are the dominant methods for fabricating SnO$_2$ ETLs in PSCs [21–23]. The fabrication of ETLs in photovoltaic devices is paramount for limiting production costs because of the requirements for its production, such as thermal treatment, multiple processing steps, operation control, and scalable processing.

Here, we report on the synthesis and ETL application of SnO$_2$ thin films on fluorine-doped tin oxide (FTO) by ED. Among the available methods, electrodeposition has the advantages of reduced production cost and large-scale manufacturing because it does not require a vacuum environment or complex operation control. Considering that perovskite materials are suitable for roll-to-roll manufacturing, the application of electrodeposition to obtain SnO$_2$ ETLs will demonstrate not only a simple, cost-effective, and scalable strategy for alternative ETLs but also facilitate development of a continuous roll-to-roll process for industrial application of PSCs.

Methods
Preparation of SnO$_2$ Film
A chronovoltammetry technique (VSP 200, Biologic) was used for ED of Sn nanospheres onto an FTO substrate using a standard three-electrode system in a deionized water solution (50 mL) containing 0.05 M SnCl$_2$·2H$_2$O [tin chloride (П), Sigma Aldrich] and 1 mL of nitric acid (HNO$_3$, Samchun Chemical). The nanospheres were then thermally treated in air at 400 °C for 30 min to obtain SnO$_2$. The aqueous solution was stirred for 1 h at 60 °C on a hot plate. After N$_2$ purging for 10 min, the solution was used for electrodeposition. In the standard three-electrode system, FTO was used as the working electrode, and a platinum plate was used as the counter electrode. The reference electrode was a Ag/AgCl electrode (CHI111) in 1 M KCl solution.

Device Fabrication
The prepared SnO$_2$ thin films on FTO (TEC 8) were used in the fabrication of PSCs. The perovskite layer was processed in two steps. A mixture of PbI$_2$ (99.999%, Aldrich) and PbCl$_2$ (99.999%, Aldrich) was dissolved in N, N-dimethylformamide and stirred at 60 °C. The molar ratio of the precursor solution (PbI$_2$:PbCl$_2$) was 1:1 (1 M). The PbI$_2$/ PbCl$_2$ solution was spin-coated on the SnO$_2$-coated FTO at 5000 rpm for 30 s in a glove box and dried on a hotplate at 70 °C. To convert it to a perovskite material, 120 μL of methylammonium iodide solution (40 mg/mL) was loaded at 0 rpm for 35 s and then spin-coated at 3500 rpm for

20 s; the sample was then annealed isothermally at 105 °C for 75 min in the ambient environment. After annealing, the films were moved into the glove box in N$_2$ atmosphere, and a hole-transporting material (HTM) was spin-coated on the MAPbI$_{3-x}$Cl$_x$/SnO$_2$/FTO film at 3000 rpm for 30 s. Poly[bis(4-phenyl)(2,4,6-trimethylphenyl)amine] (EM Index) solution (20 mg/1 mL) was used as the HTM with 15 μL of Li-bis(trifluoromethanesulfonyl)imide)/ acetonitrile (170 mg/1 mL) and 15 μL of tert-butylpyrridine. Finally, Au was deposited via thermal evaporation. TiCl$_4$ hydrolysis treatment was applied by immersing the electrodeposited SnO$_2$ films in a 40 mM TiCl$_4$ solution at 70 °C for 30 min and drying them at 150 °C in air.

Characterization
Cyclic voltammetry (CV, scan rate 50 mV/s) measurements were made to confirm the electrochemical behavior of the SnCl$_2$·2H$_2$O solution from –1.5 to 2 V. The crystalline structure of the samples was characterized by X-ray diffraction (XRD, Rigaku, Dmax 2200, Cu Kα) and X-ray photoelectron spectroscopy (XPS, ULVAC-PHI 5000, VersaProbe II). The morphologies of the samples were observed by field emission scanning electron microscopy (SEM, Hitachi S4800). The J–V curves of the PSCs were obtained using an electrochemical station (VSP200, Bio-Logic) under 100 mW/cm^2 AM 1.5G light (Sun 3000 class AAA, ABET Technology) with a metal mask 0.098 cm^2 in area. Devices were scanned at a 20 mV/s scan rate. CV measurements of the blocking layer effect were performed using a three-electrode setup after nitrogen purging for 10 min. The aqueous electrolyte contained 0.5 M KCl and the electron redox couple K$_4$[Fe(II)(CN)$_6$]/K$_3$[Fe(III)(CN)$_6$] at a concentration of 5 mM. A Ag/AgCl electrode was used for the reference electrode, and a Pt wire was used for the counter electrode; the scan rate was 50 mV/s. An Oriel-calibrated Si solar cell (SRC-1000-TC-KG5-N) was used to adjust the light intensity to one-sun illumination. The external quantum efficiency (EQE) was measured using an Ivium potentiostat and a monochromator (DongWoo Optron Co., Ltd.) under a light support (ABET 150 W xenon lamp, ABET Technology). EQE data were acquired in DC mode. Photoluminescence (PL) spectra were measured using a luminescence spectrometer (LS 55, PerkinElmer) with excitation at 530 nm. The intensity-modulated photocurrent and photovoltage were measured by an Ivium potentiostat with a Modulight LED (Ivium).

Results and Discussion
We performed CV measurements of the SnCl$_2$·2H$_2$O solution to identify suitable potential values. Figure 1a shows the CV curve, which was scanned from 2.0 to
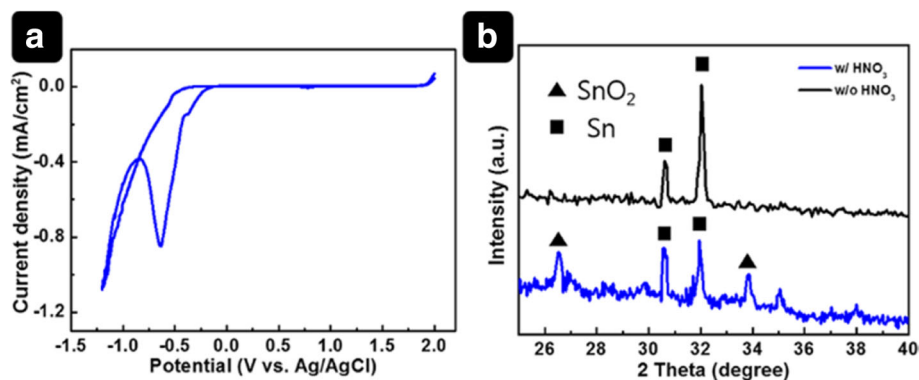
Ko et al. Nanoscale Research Letters (2017) 12:498

Page 3 of 7

Fig. 1 (**a**) CV curve measured at a scan rate of 50 mV/s and (**b**) XRD patterns of electrodeposited SnO_2

−1.2 V. All potential values were recorded with respect to the reference electrode (Ag/AgCl). As shown in Fig. 1a, an increase in the cathodic current was observed from −0.5 to −1.2 V. Generally, when the voltage is swept in a CV experiment from positive to negative voltage, the current first increases because of an electrochemical reaction on the working electrode surface and then decreases owing to local depletion of the chemical species close to the working electrode.

On the basis of the CV result, we performed ED using a chronovoltammetry technique. Note that the phase of the deposits depends on the concentration ratio of $[HNO_3]$ to $[Sn^{2+}]$ because nitric acid acts as an oxygen source in the phase [24]. The presence of HNO_3 (as identified in the XRD pattern, Fig. 1b) facilitated generation of a SnO_2–Sn co-phase. This will be referred to as SnO_2–Sn nanospheres to distinguish it from pure SnO_2. Figure 2 shows SEM images of the SnO_2–Sn nanospheres deposited on FTO substrates at different potential values (−0.5, −0.6, −0.7, −0.8, −0.9, and −1 V). We found that the applied voltage is a very important

parameter in the electrodeposition process, as the morphologies of the deposits were dramatically different. For relatively low absolute potentials (−0.5 and −0.6 V), few SnO_2–Sn nanospheres formed. On the other hand, the FTO was overlaid with Sn having irregular shapes at −0.9 and −1 V. Even though comparable SnO_2–Sn nanosphere formation occurred at −0.7 and −0.8 V, the uniformity was better at −0.7 V. As a result of these observations, −0.7 V was chosen as a suitable potential for electrodeposition of SnO_2–Sn nanospheres.

A potential of −0.7 V was also used to optimize the deposition time in the range of 150 to 210 s. Figure 3 shows SEM images of samples obtained at various deposition times and the corresponding device performance. Fewer particles formed at 150 s than at 180 s. For a longer deposition time (210 s), aggregation of SnO_2–Sn nanospheres was confirmed. To evaluate the photovoltaic performance of PSCs with the electrodeposited SnO_2 films, the SnO_2–Sn nanosphere films were thermally treated in air at 450 °C for 30 min to obtain fully converted SnO_2 films. A $CH_3NH_3PbI_{3-x}Cl_x$ perovskite
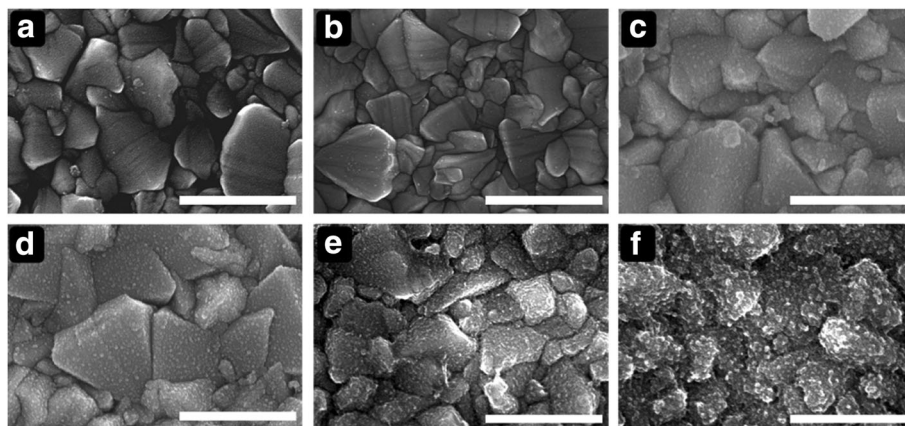

Fig. 2 Top-view SEM images of SnO_2 films electrodeposited at various applied voltages. (**a**) − 0.5 V, (**b**) −0.6 V, (**c**) −0.7 V, (**d**) −0.8 V, (**e**) −0.9 V, and (**f**) −1.0 V vs. Ag/AgCl. *Scale bar* is 1 μm

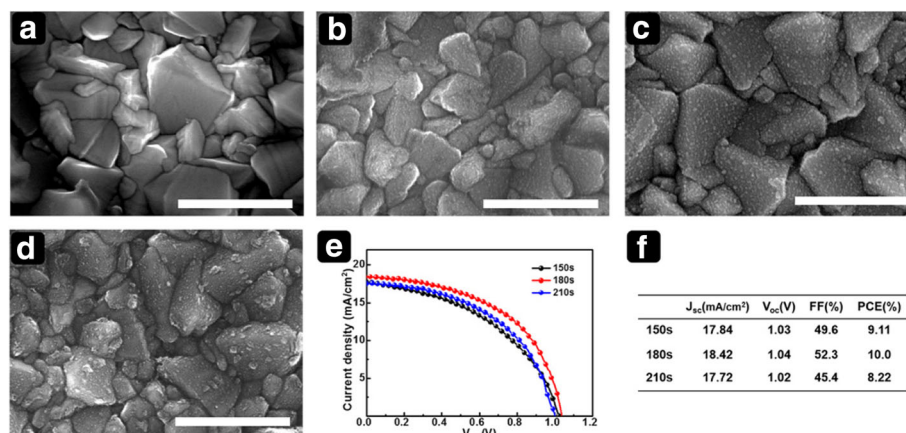Ko et al. Nanoscale Research Letters (2017) 12:498

Page 4 of 7

Fig. 3 Top-view SEM images of substrates for different deposition time. (**a**) Bare FTO and SnO$_2$ films deposited for (**b**) 150 s, (**c**) 180 s, and (**d**) 210 s. Corresponding photovoltaic performance: (**e**) J–V curves and (**f**) photovoltaic parameters of PSCs with electrodeposited SnO$_2$ ETL. *Scale bar* is 1 μm

layer was fabricated via a PbICl-seed-layer-assisted inter-diffusion process. Details are provided in the experimental section. As shown in Fig. 3e, f, for a deposition time of 150 s, the short-circuit current density (J_{sc}), open-circuit voltage (V_{oc}), fill factor (FF), and PCE (%) were 17.84 mA/cm^2, 1.03, 0.496, and 9.11%, respectively. As the deposition time increased from 150 to 180 s, J_{sc} improved, and a higher PCE of 10.0 was obtained. The use of a deposition time of 210 s mainly affected the J_{sc} and FF value, leading to a lower PCE of 8.22. To gain further insight into parasitic resistances, we calculated series resistance (R_s) and shunt resistance (R_{sh}) from the J–V curves. R_s values are 10.4, 5.2, and 12.5 (ohm cm^2); R_{sh} values are 194.9, 558.5, and 167.1 (ohm cm^2) for the time of 150, 180, and 210 s, respectively. The calculated parasitic resistances explain device performances in operation obtained from different electrochemical deposition condition. As shown in the SEM image in

Fig. 3d, the poor morphology of the SnO$_2$ film at a deposition time of 210 s is expected to impede charge transfer between CH$_3$NH$_3$PbI$_{3-x}$Cl$_x$ and FTO, resulting in a reduced J_{sc}.

Considering that the electrodeposition process depends on the ion mobility in an electrolyte solution, we also explored the effect of temperature on the morphology of the films. Figure 4 shows top-view SEM images of films deposited at different bath temperatures with −0.7 V for 180 s. As expected, the surface morphology of the SnO$_2$–Sn nanospheres prepared at different bath temperatures varies. The nanosphere size, roughness, and thickness seem to be affected, as the migration of Sn^{2+} ions was enhanced at higher temperature. The photovoltaic efficiency of PSCs fabricated using these films is compared in Fig. 4e, f. A finer SnO$_2$ film yields better performance, and the optimum efficiency was obtained for the film deposited at 60 °C. The SnO$_2$ film
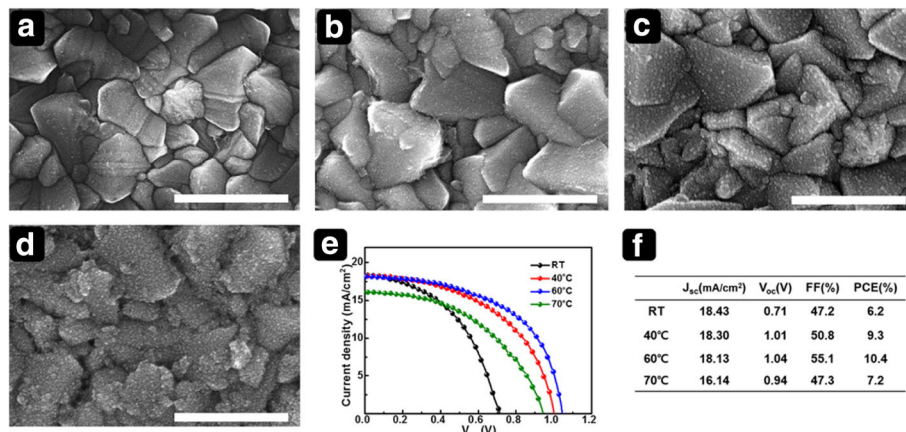

Fig. 4 Top-view SEM images of SnO$_2$ films electrodeposited at various bath temperatures. (**a**) RT, (**b**) 40 °C, e(**c**) 60 °C, and (**d**) 70 °C. Corresponding photovoltaic performance: (**e**) J–V curves and (**f**) photovoltaic parameters of PSCs with electrodeposited SnO$_2$ ETL. *Scale bar* is 1 μm

Ko *et al. Nanoscale Research Letters* (2017) 12:498

Page 5 of 7

morphology is expected to significantly affect the PSC performance because planar PSCs have a direct interface between the ETL and the perovskite layer. The improved conformality could result in good contact that affords enhanced electron transport [25]. The SEM images of perovskite layer fabricated from varied ETLs were provided in supporting information (SI) Additional file 1: Figure S1.
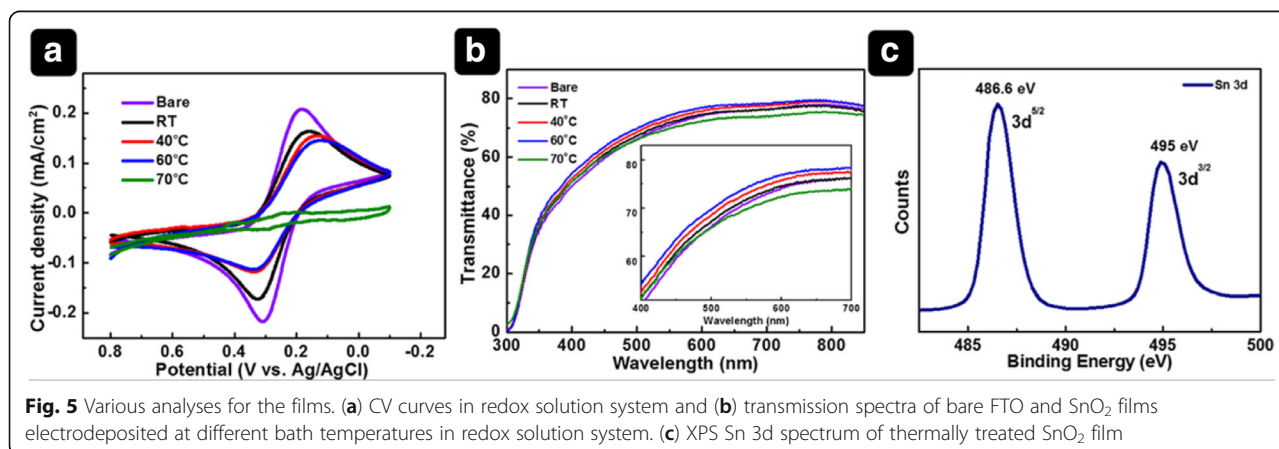
To further examine the effect of temperature on the morphology with respect to the blocking effect of the electrodeposited SnO_2 films, we conducted CV measurements in an aqueous electrolyte containing $[Fe(CN)_6]^{3-}/[Fe(CN)_6]^{4-}$ because the redox reaction depends on charge transfer between the FTO and the electrolyte [26]. The electron transfer kinetics can be interpreted by extracting the separation of the peak potentials and peak current of a redox system from the CV curves. If the redox reaction between $[Fe(CN)_6]^{3-}/[Fe(CN)_6]^{4-}$ ions is hampered by the SnO_2 layer, the oxidized and reduced forms of the redox couple exhibit peak potentials that are shifted away from the control on bare FTO and become semireversible; consequently, the peak current density will be reduced [27]. Figure 5a shows the CV curves of bare FTO and the SnO_2 films. The CV curve of bare FTO clearly shows a reversible redox reaction, indicating a lower barrier to electron transfer. In contrast, the FTO with electrodeposited SnO_2 exhibits a larger peak-to-peak separation (ΔE_p) of the cathodic and anodic peak potentials compared to that of bare FTO. The ΔE_p values of films deposited at room temperature (RT), 40, 60, and 70 °C are 125, 175, 207, and 230 mV, respectively. This indicates that the kinetics of the redox reaction are changed by the blocking effect of the SnO_2 films. In contrast, charge transfer at the FTO is highly suppressed by the film deposited at 70 °C, implying that the SnO_2 is densely deposited onto the FTO. The thick SnO_2 film could result in less effective and slower electron transport, negatively affecting the photovoltaic performance. The cathodic peak current (I_p) of the films

decreased with increasing bath temperature, indicating that the FTO coverage was improved.

On the basis of the CV results and SEM images, we could speculate that the FTO electrode at low temperature is covered with fewer nanoparticles; therefore, we conclude that the SnO_2 film fabricated at 60 °C has a suitable thickness and morphology for use in PSCs and has a dominant effect on the device performance. The optical transmission of the SnO_2 films is also compared (Fig. 5b). As the bath temperature increases from RT to 60 °C, the transmittance of the SnO_2 films is enhanced compared to that of FTO. At a high bath temperature of 70 °C, the transmittance is inferior to that of FTO, which is attributed to the increased film thickness, as evidenced by the SEM image.

XPS was performed to measure the composition of the electrodeposited films. The XPS spectrum of the thermally treated SnO_2 film is shown in Fig. 5c. Sn $3d_{5/2}$ and Sn $3d_{3/2}$ peaks at binding energies of 486.6 and 495 eV, respectively, were observed, whereas the film without heat treatment showed Sn $3d_{5/2}$ and Sn $3d_{3/2}$ peaks at 484.8 and 493.2 eV, respectively (SI, Additional file 1: Figure S2) [21]. The SnO_2 film is clearly obtained through heat treatment.

On the other hand, although SnO_2 electrodeposition provides a versatile and low-cost route toward scalable manufacturing systems [28], the demonstrated photovoltaic performance of the electrodeposited SnO_2 films is not impressive. To improve the device performance, $TiCl_4$ treatment was used to modify the SnO_2 surface. As shown in Fig. 6a, the device based on SnO_2 without $TiCl_4$ treatment shows a J_{sc} value of 18.12 mA/cm², a V_{oc} value of 1.04 V, a FF of 57.3%, and a PCE of 10.83%. In comparison, the device based on SnO_2 with $TiCl_4$ treatment (SnO_2–$TiCl_4$) exhibits a J_{sc} value of 18.65 mA/cm², a V_{oc} value of 1.02 V, a FF of 79.1%, and a PCE of 14.97% (a 38% enhancement). The efficiency improvement is attributed mainly to the improved J_{sc} and FF.
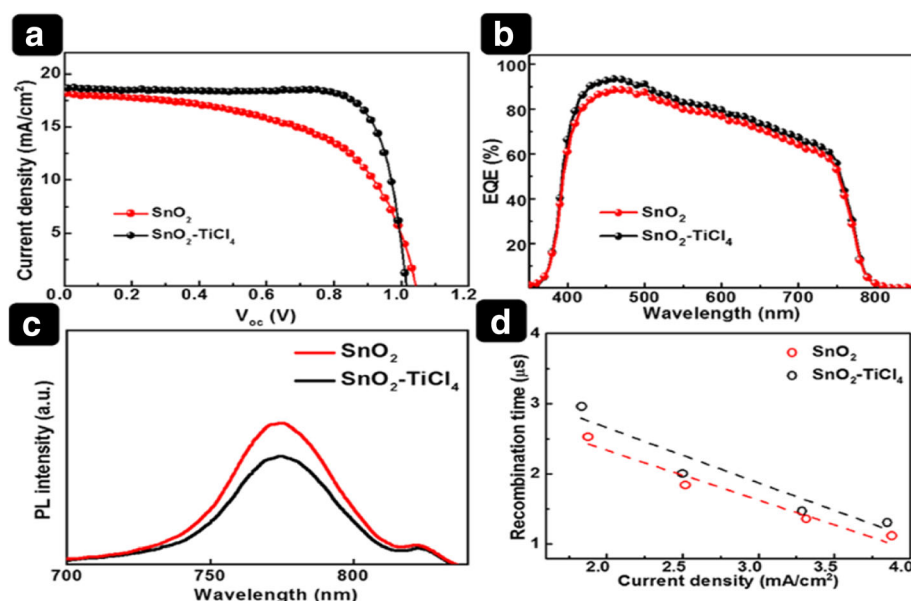

Fig. 5 Various analyses for the films. (**a**) CV curves in redox solution system and (**b**) transmission spectra of bare FTO and SnO_2 films electrodeposited at different bath temperatures in redox solution system. (**c**) XPS Sn 3d spectrum of thermally treated SnO_2 film

Ko *et al. Nanoscale Research Letters* (2017) 12:498

Page 6 of 7

Fig. 6 Cell performance with IPCE and PL data. (**a**) *J–V* curves and (**b**) EQE spectra of PSC devices based on SnO_2 and SnO_2–$TiCl_4$. (**c**) Steady-state PL spectra of FTO/SnO_2/perovskite and FTO/SnO_2-$TiCl_4$/perovskite samples. (**d**) Recombination time versus current density

To understand the mechanism by which $TiCl_4$ treatment improves the J_{sc} value, we measured the EQE (Fig. 6b). The EQE of the SnO_2–$TiCl_4$ device shows an increase from 17.8 to 18.6 mA/cm^2 in the entire wavelength spectral region. The enhancement in the EQE after $TiCl_4$ treatment is in good agreement with the improved J_{sc} in the *J–V* curves, which implies efficient charge collection. The EQE enhancement is expected to be originated from a better injection of electrons at the ETLs/perovskite interface [29, 30]. To further investigate the electron injection, the steady-state PL was measured for substrates with both ETLs. Figure 6c shows the PL spectra of the FTO/SnO_2/perovskite and FTO/SnO_2–$TiCl_4$/perovskite samples. Compared to the SnO_2-based film, the SnO_2–$TiCl_4$-based film exhibited reduced PL intensity, indicating that electron transfer from the perovskite to the ETL was enhanced by $TiCl_4$ treatment since the PL emission of perovskite layer is quenched by contact. Possibly, the enhanced electron injection in ETLs with $TiCl_4$ treatment improved the EQE. To further examine the improved performance of the SnO_2–$TiCl_4$-based device, intensity-modulated photovoltage spectroscopy (IMVS, Additional file 1: Figure S3) was performed to characterize the recombination time (τ_r) (Fig. 6d). The recombination lifetime depends on the concentration of charge carriers in the solar cell. Thus, the recombination time is influenced by the current density, which is modulated by varying the light intensity. The carrier recombination time for the SnO_2–$TiCl_4$-based device was 1.17 times longer than that of the SnO_2-based devices. The longer time

constant for recombination is expected to afford an increase in J_{sc}, FF, and better device performance [31, 32]. The device statistics (30 samples for each) were provided in Additional file 1: Figure S4.

Conclusions

In summary, we demonstrated a versatile and scalable electrodeposition technique to obtain a SnO_2 ETL for planar heterojunction PSCs. The properties of the electrodeposited SnO_2 depended strongly on the deposition time, electrolyte bath temperature, and applied voltage. Moreover, devices based on SnO_2 treated with $TiCl_4$ showed significantly enhanced V_{oc} and J_{sc}, leading to a PCE enhancement of 42%.

Additional file

Additional file 1: Figure S1. SEM images of perovskite layer prepared from varied ETLs. (a) RT of SnO_2, (b) 40℃ of SnO_2, (c) 60℃ of SnO_2, (d) 70℃ of SnO_2, and (e) 60℃ of SnO_2-$TiCl_4$. Figure S2 XPS spectrum of SnO_2 film without thermal treatment. Figure S3 IMVS curves of (a) SnO_2-based and (b) SnO_2–$TiCl_4$-based devices. Figure S4 Performance statistic of devices based on different ETLs. (DOCX 3379 kb)

Ko *et al. Nanoscale Research Letters* (2017) 12:498

Page 7 of 7

Publisher's Note
Springer Nature remains neutral with regard to jurisdictional claims in published maps and institutional affiliations.

Author details
[1]Department of Materials Chemistry and Engineering, Department of Energy Engineering, Konkuk University, Seoul 143-701, Republic of Korea. [2]IT Materials Technology Research Section, ETRI, Gajeongro 218, Yuseong, Daejeon, Republic of Korea.

References
1. Kojima A, Teshima K, Shirai Y, Miyasaka T (2009) Organometal halide perovskites as visible-light sensitizers for photovoltaic cells. J Am Chem Soc 131(17):6050–6051. doi:10.1021/ja809598r
2. Ke W, Fang G, Liu Q, Xiong L, Qin P, Tao H, Wang J, Lei H, Li B, Wan J, Yang G, Yan Y (2015) Low-temperature solution-processed tin oxide as an alternative electron transporting layer for efficient perovskite solar cells. J Am Chem Soc 137(21):6730–6733. doi:10.1021/jacs.5b01994
3. Saliba M, Matsui T, Domanski K, Seo J-Y, Ummadisingu A, Zakeeruddin SM, Correa-Baena J-P, Tress WR, Abate A, Hagfeldt A, Grätzel M (2017) Incorporation of rubidium cations into perovskite solar cells improves photovoltaic performance. doi:10.1126/science.aah5557
4. Miyata A, Mitioglu A, Plochocka P, Portugall O, Wang JT-W, Stranks SD, Snaith HJ, Nicholas RJ (2015) Direct measurement of the exciton binding energy and effective masses for charge carriers in organic–inorganic tri-halide perovskites. Nat Phys 11(7):582–587. doi:10.1038/nphys3357
5. Xing G, Mathews N, Sun S, Lim SS, Lam YM, Grätzel M, Mhaisalkar S, Sum TC (2015) Long-range balanced electron and hole-transport lengths in organic-inorganic MAPbI3. Science 324. doi:10.1126/science.1243167
6. Stranks SD, Eperon GE, Grancini G, Menelaou C, MJP A, Leijtens T, Herz LM, Petrozza A, Snaith HJ (2013) Electron-hole diffusion lengths exceeding 1 micrometer in an organometal trihalide perovskite absorber. Science 342(6156):341–344. doi:10.1126/science.1243982
7. Meng L, You J, Guo TF, Yang Y (2016) Recent advances in the inverted planar structure of perovskite solar cells. Acc Chem Res 49(1):155–165. doi:10.1021/acs.accounts.5b00404
8. Park NG (2016) Methodologies for high efficiency perovskite solar cells. Nano Convergence 3(1):15. doi:10.1186/s40580-016-0074-x
9. Jeon NJ, Noh JH, Kim YC, Yang WS, Ryu S, Seok SI (2014) Solvent engineering for high-performance inorganic-organic hybrid perovskite solar cells. Nat Mater 13(9):897–903. doi:10.1038/nmat4014
10. Heo JH, You MS, Chang MH, Yin W, Ahn TK, Lee S-J, Sung S-J, Kim DH, Im SH (2015) Hysteresis-less mesoscopic CH3NH3PbI3 perovskite hybrid solar cells by introduction of Li-treated TiO2 electrode. Nano Energy 15:530–539. doi:10.1016/j.nanoen.2015.05.014
11. Ito S, Tanaka S, Manabe K, Nishino H (2014) Effects of surface blocking layer of Sb2S3on nanocrystalline TiO2for CH3NH3PbI3Perovskite solar cells. J Phys Chem C 118(30):16995–17000. doi:10.1021/jp500449z
12. Hui-Chi Chiu C-SY (2007) Hydrothermal synthesis of SnO2 nanoparticles and their gas-sensing of alcohol. J Phys Chem 111:7256–7259. doi:10.1021/jp0688355
13. Yasuhiro Tachibana KH, Takano S, Sayama K, Arakawa H (2002) Investigations on anodic photocurrent loss processes in dye sensitized solar cells: comparison between nanocrystalline SnO2 and TiO2 films. Chem Phys Lett 364:297–302
14. Aziz M, Abbas SS, Baharom WRW, Mahmud WZW (2012) Structure of SnO2 nanoparticles by sol–gel method. Mater Lett 74:62–64. doi:10.1016/j.matlet.2012.01.073
15. Wang D, Chu X, Gong M (2006) Gas-sensing properties of sensors based on single-crystalline SnO2 nanorods prepared by a simple molten-salt method. Sensors Actuators B Chem 117(1):183–187. doi:10.1016/j.snb.2005.11.022
16. Krishnakumar T, Jayaprakash R, Parthibavarman M, Phani AR, Singh VN, Mehta BR (2009) Microwave-assisted synthesis and investigation of SnO2 nanoparticles. Mater Lett 63(11):896–898. doi:10.1016/j.matlet.2009.01.032
17. Chen Z, Tian Y, Li S, Zheng H, Zhang W (2012) Electrodeposition of arborous structure nanocrystalline SnO2 and application in flexible dye-sensitized solar cells. J Alloys Compd 515:57–62. doi:10.1016/j.jallcom.2011.10.116
18. Lee K-T, Lu S-Y (2012) Porous FTO thin layers created with a facile one-step Sn4+–based anodic deposition process and their potential applications in ion sensing. J Mater Chem 22(32):16259. doi:10.1039/c2jm33060a
19. Lee K-T, Lu S-Y (2013) One-step Sn4+–based anodic deposition for flattening of fluorine-doped tin oxide enabling large transmittance enhancements. RSC Adv 3(23):9011. doi:10.1039/c3ra40416a
20. Chu D, Masuda Y, Ohji T, Kato K (2011) Fast synthesis, optical and bio-sensor properties of SnO2 nanostructures by electrochemical deposition. Chem Eng J 168(2):955–958. doi:10.1016/j.cej.2011.02.029
21. Ren X, Yang D, Yang Z, Feng J, Zhu X, Niu J, Liu Y, Zhao W, Liu SF (2017) Solution-processed Nb: SnO2 electron transport layer for efficient planar perovskite solar cells. ACS Appl Mater Interfaces 9(3):2421–2429. doi:10.1021/acsami.6b13362
22. Correa Baena JP, Steier L, Tress W, Saliba M, Neutzner S, Matsui T, Giordano F, Jacobsson TJ, Srimath Kandada AR, Zakeeruddin SM, Petrozza A, Abate A, Nazeeruddin MK, Grätzel M, Hagfeldt A (2015) Highly efficient planar perovskite solar cells through band alignment engineering. Energy Environ Sci 8(10):2928–2934. doi:10.1039/c5ee02608c
23. Chen H, Liu D, Wang Y, Wang C, Zhang T, Zhang P, Sarvari H, Chen Z, Li S (2017) Enhanced performance of planar perovskite solar cells using low-temperature solution-processed al-doped SnO2 as electron transport layers. Nanoscale Res Lett 12(1):238. doi:10.1186/s11671-017-1992-1
24. Chen X, Liang J, Zhou Z, Duan H, Li B, Yang Q (2010) The preparation of SnO2 film by electrodeposition. Mater Res Bull 45(12):2006–2011. doi:10.1016/j.materresbull.2010.07.029
25. Roelofs KE, Pool VL, Bobb-Semple DA, Palmstrom AF, Santra PK, Van Campen DG, Toney MF, Bent SF (2016) Impact of conformality and crystallinity for ultrathin 4 nm compact TiO2 layers in perovskite solar cells. Adv Mater Interfaces 3(21):1600580. doi:10.1002/admi.201600580
26. Moehl T, Im JH, Lee YH, Domanski K, Giordano F, Zakeeruddin SM, Dar MI, Heiniger LP, Nazeeruddin MK, Park NG, Gratzel M (2014) Strong photocurrent amplification in perovskite solar cells with a porous TiO2 blocking layer under reverse bias. J Phys Chem Letters 5(21):3931–3936. doi:10.1021/jz502039k
27. Harnisch F, Freguia S (2012) A basic tutorial on cyclic voltammetry for the investigation of electroactive microbial biofilms. Chem Asian J 7(3):466–475. doi:10.1002/asia.201100740
28. Vequizo JJM, Wang J, Ichimura M (2010) Electrodeposition of SnO2Thin films from aqueous tin sulfate solutions. Jpn J Appl Phys 49(12):125502. doi:10.1143/jjap.49.125502
29. Liu D, Li S, Zhang P, Wang Y, Zhang R, Sarvari H, Wang F, Wu J, Wang Z, Chen ZD (2017) Efficient planar heterojunction perovskite solar cells with Li-doped compact TiO 2 layer. Nano Energy 31:462–468. doi:10.1016/j.nanoen.2016.11.028
30. Agresti A, Pescetelli S, Cinà L, Konios D, Kakavelakis G, Kymakis E, Carlo AD (2016) Efficiency and stability enhancement in perovskite solar cells by inserting lithium-neutralized graphene oxide as electron transporting layer. Adv Funct Mater 26(16):2686–2694. doi:10.1002/adfm.201504949
31. Li S, Zhang P, Wang Y, Sarvari H, Liu D, Wu J, Yang Y, Wang Z, Chen ZD (2016) Interface engineering of high efficiency perovskite solar cells based on ZnO nanorods using atomic layer deposition. Nano Res 10(3):1092–1103. doi:10.1007/s12274-016-1407-0
32. Li S, Zhang P, Chen H, Wang Y, Liu D, Wu J, Sarvari H, Chen ZD (2017) Mesoporous PbI2 assisted growth of large perovskite grains for efficient perovskite solar cells based on ZnO nanorods. J Power Sources 342:990–997. doi:10.1016/j.jpowsour.2017.01.024